Numerical Modeling of Thermo-Mechanically Induced Stress in Substrates for Droplet-Based Additive Manufacturing Processes

Chang Yoon Park
Department of Mechanical Engineering,
University of California,
Berkeley, CA 94720
e-mail: changyoonpark@berkeley.edu

Tarek I. Zohdi
Department of Mechanical Engineering,
University of California,
Berkeley, CA 94720
e-mail: zohdi@berkeley.edu

Within the scope of additive manufacturing (AM) methods, a large number of popular fabrication techniques involve high-temperature droplets being targeted to a substrate for deposition. In such methods, an "ink" to be deposited is tailor-made to fit the desired application. Concentrated stresses are induced on the substrate in such procedures. A numerical simulation framework that can return quantitative and qualitative insights regarding the mechanical response of the substrate is proposed in this paper. A combined smoothed particle hydrodynamics (SPH)-finite element (FE) model is developed to solve the governing coupled thermo-mechanical equations, for the case of Newtonian inks. We also highlight the usage of consistent SPH formulations in order to recover first-order accuracy for the gradient and Laplacian operators. This allows one to solve the heat-equation more accurately in the presence of free-surfaces. The proposed framework is then utilized to simulate a hot droplet impacting a flat substrate. [DOI: 10.1115/1.4043254]

1 Introduction

Additive manufacturing (AM) methods are becoming common choice for fabricating cutting edge devices. AM broadly covers various methods that involve droplets being deposited onto a surface, such as droplet based manufacturing (DBM) [1], ink-jet printing [2,3], LIFT (laser-induced forward transfer, [4–6]) and direct ink writing (DIW, [7]). In some cases, the droplets may be laden with extremely fine micro or nano materials tailored to each specific application, where good examples are given in Refs. [8,9]. Despite the considerable amount of recent advancement in additive manufacturing technologies, the development of numerical frameworks that may be applied to such methods has been mostly stagnant.

When the targeted substrate is expected to be fragile, the integrity of the substrate during the deposition process is critical for the engineer. During the process, the induced stress within the substrate is highly dependent on both heat transfer and momentum transfer between the droplet and the substrate.

In most cases, observations can only be made after a resource consuming experimental process [10–13]. We propose a new numerical framework, based directly on the continuum equations involved in such processes. The proposed numerical framework involves a thermo-mechanical solution solved via SPH (smoothed particle hydrodynamics) and a one-way coupled finite element method (FEM) setup which is used to compute the thermal/mechanical stress induced in the impacted solid. Advantages of such an approach includes:

- Computationally affordable simulation of the free-surface fluid object (droplet).
- Rapidly deforming free-surfaces of the fluid object is trivially represented.
- Obviates the difficulties due to time step differences within the solid domain and the fluid domain.

During the process, the geometry of the fluid droplet undergoes rapid deformation. A mesh-based method (such as the finite element method) will be very expensive for such problems, due to the re-meshing process that will be required after each time step. Thus, a mesh-free method such as SPH can be an appropriate alternative approach. The main intention of this paper is to provide an effective numerical framework that can assist the engineer designing a droplet-based manufacturing process (Fig. 1).

This paper is organized as follows. *First*, we state the governing equations of the problem. *Second*, a detailed explanation regarding the proposed discretization of the governing equations, for a Newtonian-type ink, is given. *Third*, a numerical convergence study is performed to justify the usage of the framework. *Fourth*, a practical numerical example is provided to illustrate the method, along with a brief comparison against a previously developed predictive model regarding heat penetration. Finally, we mention some limitations of the proposed approach, which will be investigated in future work.

Remark. In some applications, the composition of the ink may dictate the viscous behavior the ink. The droplet must be modeled as a non-Newtonian fluid in this case. While the topic regarding solving non-Newtonian flows with SPH exceeds the scope of this paper, a brief note regarding the solution process for such problems will be given later in this paper.

2 Governing Equations

2.1 Navier–Stokes Equation for Newtonian Fluids. The incompressible Navier–Stokes equations in Lagrangian formalism
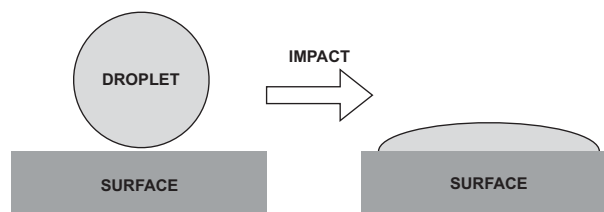

Fig. 1 Droplet impacting a surface

are the field equations:

$$\frac{D\mathbf{r}}{Dt} = \mathbf{u} \tag{1}$$

$$\nabla \cdot \mathbf{u} = 0 \tag{2}$$

$$\rho \frac{D\mathbf{u}}{Dt} = \nabla \cdot \boldsymbol{\sigma}_f + \rho \mathbf{g} \tag{3}$$

where for a Newtonian fluid

$$\boldsymbol{\sigma}_f = -p\mathbf{1} + \mu \nabla^2 \mathbf{u} \tag{4}$$

where $\mathbf{r}$ and $\mathbf{u}$ are the position vector and the velocity vector, respectively, ρ is the density of the fluid, $\mathbf{g}$ is the body force, $\boldsymbol{\sigma}_f$ is the stress tensor of the fluid, μ is the dynamic viscosity of the fluid, and p represents the pressure. Note that $D(\cdot)/Dt$ represents the material derivative.

SPH is a mesh-free numerical method that can be used to discretize various continuum mechanics problems. Originally intended for astrophysical problems, SPH found many practical usage cases in analyzing fluid flows involving free-surfaces [14–16]. The set of equations given by SPH is usually closed with a weakly compressible scheme in which the pressure term is directly correlated with the density variable through an equation of state, which is used throughout this paper:

$$p = \frac{1}{\gamma} \rho_0 c_0^2 \left(\left(\frac{\rho}{\rho_0} \right)^{\gamma} - 1 \right) \tag{5}$$

where ρ_0 represents the reference density, c_0 represents the speed of sound, and γ is a constant, usually chosen to be 7. This type of equation of state is typically known as a variant of Tait's equation of state, and is widely used in the SPH community.

For the problem in interest, Equation (3) should incorporate the surface tension, where its effect may be significant in microscale droplets:

$$\rho \frac{D\mathbf{u}}{Dt} = \nabla \cdot \boldsymbol{\sigma}_f + \rho \mathbf{g} + \underbrace{\mathbf{f^s}}_{\text{Surface Tension}} \tag{6}$$

There are two popular methods for implementing surface tension. In the context of SPH, one method originally proposed by Morris [17] takes the following form:

$$\rho \frac{D\mathbf{u}}{Dt} = \nabla \cdot \boldsymbol{\sigma}_f + \rho \mathbf{g} + \underbrace{\delta_s \kappa \varsigma \mathbf{n}}_{\text{Surface Tension}} \tag{7}$$

where ς is the surface tension coefficient of the fluid–air interface, κ is the curvature of the free-surface, and $\mathbf{n}$ is the surface normal defined at $\mathbf{x}_j$. Also, δ_s is a function such that

$$\delta_s(\mathbf{x}) = \begin{cases} 1, & \mathbf{x} \in \Omega_{FS} \\ 0, & \mathbf{x} \in \Omega_I \end{cases} \tag{8}$$

where Ω_{FS} represents the subset of the fluid domain located on the free-surface and Ω_I represents the subset of the fluid domain located in the interior, so that $\mathbf{x} \in \Omega_{FS} \cup \Omega_I = \Omega$ and $\Omega_{FS} \cap \Omega_I = \varnothing$. This is often called the continuum surface force (CSF) surface tension model introduced in Ref. [17].

The method has several drawbacks. To accurately evaluate the surface curvature, it is advantageous that kernel truncation does not occur near the free surface. To alleviate errors due to such a truncation, it is thus required to model the surrounding medium (such as air) with a separate set of SPH particles. The method also is reported to return surface curvatures with large errors [18] when particles are sparsely distributed (such as small detached droplets).

Another method to model surface tension is the IIF (inter-particle interaction force) model, which directly adds forces between the SPH particles that represent attraction/repulsion forces due to

molecular interactions [19]. The forces only act on the particles near the free surface since the forces cancel each other out in the interior of the fluid. Since the force is not derived from a continuum model, the force must be calibrated to bridge the scale between the SPH and the molecular particles. When calibrated, the model accurately reproduces surface tension effects, without the computation of the free-surface curvature, which is prone to generate numerical errors. In Ref. [19], the authors employ the following interaction model:

$$\mathbf{f}_{ij}^s = \begin{cases} s_{ij} \cos\left(\frac{1.5\pi}{3h} r_{ij}\right) \mathbf{e}_{ji}, & r_{ij} \leq h \\ 0, & r_{ij} > h \end{cases} \tag{9}$$

where s_{ij} is a parameter used to calibrate the surface tension model. In this paper, we propose a modified form of this interaction model that weighs the interaction force with the mass m_i, in order to account for the difference in mass, with s as a calibration parameter and that exactly conserves linear momentum:

$$\mathbf{f}_{ij}^s = \begin{cases} s \frac{2m_i}{m_i + m_j} \cos\left(\frac{1.5\pi}{3h} r_{ij}\right) \mathbf{e}_{ji}, & r_{ij} \leq h \\ 0, & r_{ij} > h \end{cases} \tag{10}$$

2.2 Thermo-Elasticity. For the purpose of this work, we assume that the deformation of the solid due to change in temperature and momentum transfer from the fluid droplet is small. We also consider the timescale of the momentum transfer process to be significantly longer than the timescale of the shock waves traveling throughout the solid (which is directly correlated with the speed of sound in the solid). Thus, a linear-quasi-static formulation may be justified:

$$\nabla \cdot \boldsymbol{\sigma}_s = -\mathbf{f}_{ext} \tag{11}$$

$$\boldsymbol{\sigma}_s = \lambda \left(\nabla \cdot \mathbf{v} - \alpha \Delta T \left(3 + 2\frac{G}{\lambda} \right) \right) \mathbf{1} + 2G\boldsymbol{\varepsilon}(\mathbf{v}) \tag{12}$$

$$\boldsymbol{\varepsilon} = \frac{1}{2} \left(\nabla \mathbf{v} + (\nabla \mathbf{v})^T \right) \tag{13}$$

where $\boldsymbol{\sigma}_s$ is the Cauchy stress of the solid, $\mathbf{f}_{ext}$ is the external forces exerted by the impacting fluid, $\boldsymbol{\varepsilon}$ is the resulting strain, $\mathbf{u}$ are the displacements, λ is the first Lamé constant, G is the shear modulus, α is the thermal expansion coefficient, and ΔT is the increase in temperature. We employ the finite element method as described later in the paper (Fig. 2).
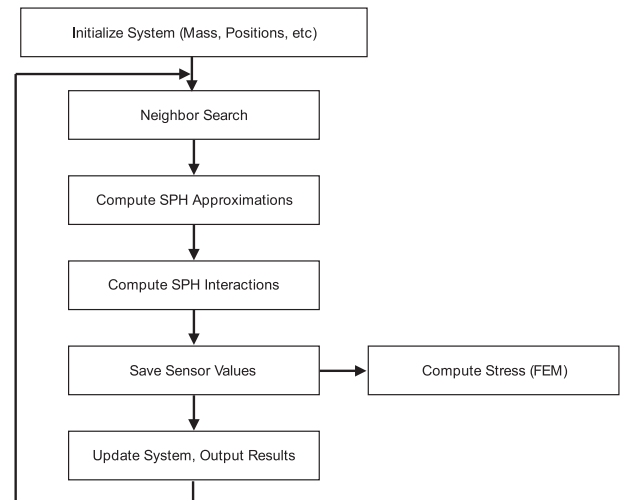

Fig. 2 Algorithmic procedures of the code

3 Discretization

3.1 Navier–Stokes.
We discretize the Navier–Stokes equation using SPH:

$$\frac{D\mathbf{u}}{Dt} = -\left\langle \frac{1}{\rho}\nabla p \right\rangle + \left\langle \frac{\mu}{\rho}\nabla^2\mathbf{u} \right\rangle + \mathbf{g} \tag{14}$$

$$\frac{D\rho}{Dt} = \langle \rho\nabla\cdot\mathbf{u} \rangle \tag{15}$$

$$p = f_{EOS}(\rho) \tag{16}$$

where $\langle\cdot\rangle$ represents the discretized version of the expression using SPH and f_{EOS} represents the equation of state. The pressure gradient contribution in Eq. (14) can be written in the symmetric form specifically found in [16]:

$$-\left\langle \frac{1}{\rho}\nabla p \right\rangle_i = -\sum_{j\in\mathcal{N}_i}\left(\frac{p_i}{\rho_i^2}+\frac{p_j}{\rho_j^2}\right)\nabla_i W_{ij}m_j \tag{17}$$

Throughout the paper, the index i represents the ith SPH particle, while $j\in\mathcal{N}_i$ represents the set of neighbors of the ith particle. W_{ij} is the kernel function centered around particle i, $\nabla_i W_{ij}$ represents the gradient of the kernel, p_i is the pressure of particle i, p_j is the pressure of particle j, ρ_i is the density of particle i, ρ_j is the density of particle j, and m_i and m_j represent the mass of particle i and j, respectively. The Quintic Wendland kernel was employed due to its superior properties when used with SPH, which was rigorously verified in Ref. [20]. As in Ref. [21], the viscosity contribution is discretized as

$$\left\langle \frac{\mu}{\rho}\nabla^2\mathbf{u} \right\rangle_i = \sum_{j\in\mathcal{N}_i}\frac{4m_j(\mu_i+\mu_j)\mathbf{r}_{ij}\cdot\nabla_i W_{ij}}{(\rho_i+\rho_j)^2(r_{ij}^2+\varepsilon)}\mathbf{u}_{ij} \tag{18}$$

The continuity equation is discretized with the method found in Ref. [22], also known as δ-SPH:

$$\langle\rho\nabla\cdot\mathbf{u}\rangle_i = -\rho_i\sum_{j\in\mathcal{N}_i}(\mathbf{u}_j-\mathbf{u}_i)\cdot\nabla_i W_{ij}V_j + \delta h c_0\mathcal{D}_i \tag{19}$$

where $\mathcal{D}_i$ is the "diffusion" term, defined as

$$\mathcal{D}_i = 2\sum_{j\in\mathcal{N}_i}\psi_{ij}\frac{\mathbf{r}_{ji}\cdot\nabla W_{ij}}{r_{ij}^2}V_j \tag{20}$$

where δ is a tunable constant (usually chosen to be 0.1), h is the SPH smoothing length, c_0 is the speed of sound, and ψ_{ij} is defined as

$$\psi_{ij} = (\rho_j-\rho_i)-\frac{1}{2}\left(\langle\nabla_1\rho_i\rangle+\langle\nabla_1\rho_j\rangle\right)\cdot\mathbf{r}_{ji} \tag{21}$$

where $\langle\nabla_1(\cdot)\rangle$ represents the renormalized gradient operator. $\langle\nabla_1\rho_i\rangle$ can then be written as

$$\langle\nabla_1\rho_i\rangle = \mathbf{B}_i\sum_{j\in\mathcal{N}(i)}(\rho_j-\rho_i)\nabla_i W_{ij}V_j \tag{22}$$

Here, $\mathbf{B}_i$ is the *first derivative renormalization matrix* suggested by Oger et al. [23], which is defined as

$$\mathbf{B}_i = \left[-\sum_{j\in\mathcal{N}(i)}\mathbf{r}_{ij}\otimes\nabla W_{ij}V_j\right]^{-1} \tag{23}$$

Physically, this term adds "artificial diffusivity" to the continuity equation. Although exact conservation of mass no longer holds, the added diffusivity greatly increases stability throughout the system.

3.2 Heat Equation.
We now represent the balance of energy for an *incompressible* fluid, also in Lagrangian formalism:

$$\rho\frac{De}{Dt} = \Phi + \nabla\cdot(k\nabla T) \tag{24}$$

Here, e is the specific energy, k is the thermal conductivity of the medium, and Φ is the dissipation function. This accounts for the dissipation that occurs in the fluid due to viscous effects, and for an *incompressible* fluid, where bulk viscosity is assumed to be negligible,

$$\Phi = 2\mu\mathbf{D}:\mathbf{D} \tag{25}$$

$$\mathbf{D} = \frac{1}{2}\left(\nabla\mathbf{u}+(\nabla\mathbf{u})^T\right) \tag{26}$$

The significance of the dissipation due to the deforming fluid for our problem is low, and is excluded in our formulation. Note that this assumption may not hold in other applications (such as lubricants in bearings). Also, since the droplet is assumed to be incompressible, temperature increase due to adiabatic compression of the fluid is ignored. Equation (24) now simplifies to

$$\rho c\frac{DT}{Dt} = \nabla\cdot(k\nabla T) \tag{27}$$

Here, c represents the specific heat capacity of the medium. The energy equations must solved for both the fluid and the solid, in order to model the heat transfer between the fluid droplet and the impacted surface. The temperature of the system is solved according to the discretized version of the heat equation:

$$\rho c\frac{DT}{Dt} = \langle\nabla\cdot(k\nabla T)\rangle \tag{28}$$

In Ref. [24], the following discretization was suggested:

$$c_i\frac{DT_i}{Dt} = \sum_{j\in\mathcal{N}_{FS}(i)}\frac{4m_j}{\rho_i\rho_j}\frac{k_ik_j}{k_i+k_j}T_{ij}\frac{\mathbf{r}_{ij}\cdot\nabla_i W_{ij}}{r_{ij}^2+\varepsilon} \tag{29}$$

Figure 3 shows a brief comparison of the two Laplacian operators on a 11×11 cartesian particle distribution representing $x=[0,1]$, $y=[0,1]$, $f(x,y)=\frac{1}{2}(x^2+y^2)$. The analytical Laplacian of $f(x,y)$ should be 2, in this case. It is a well known that when using conventional SPH operators (such as the one above), the accuracy of the Laplacian severely deteriorates and fails to recover the correct value near the free surface (Fig. 3) as mentioned in the original paper [25]. Such effects are usually ignored with justification [26] when discretizing the viscosity in Eq. (14), but accurately computing the heat transfer inside our defined geometry is an important aspect which should be addressed.

Recent advancement in SPH discretization techniques [27,28] suggests the following renormalization tensor for second derivatives, which recovers first-order accuracy of the Laplacian for an *arbitrary* distribution of SPH particles:

$$\langle\nabla_1^2 f_i\rangle = 2\mathbf{L}_i:\left[\left(\sum_{j\in\mathcal{N}_{FS}(i)}\mathbf{e}_{ij}\otimes\nabla_i W_{ij}\right)\left(\frac{f_i-f_j}{r_{ij}}-\mathbf{e}_{ij}\cdot\nabla_1 f_i\right)V_j\right] \tag{30}$$

Using the above correction, it is no longer required that the particles must retain the predefined stencil (dx) to reach convergence. Here, $\mathbf{L}_i$ is the correction tensor for the second derivative and is the solution to the following set of equations:

$$-\delta^{mn} = \sum_{j\in\mathcal{N}_{FS}(i)}(A_{kmn}^i e_{ij}^k+r_{ij}^m e_{ij}^n)(L_i^{op}+e_{ij}^o(\nabla_i W_{ij})^p V_j) \tag{31}$$

$$A_i^{kmn} = G_i^{kq}\sum_{j\in\mathcal{N}_{FS}(i)}(r_{ij}^m r_{ij}^n(\nabla_i W_{ij})^q V_j) \tag{32}$$
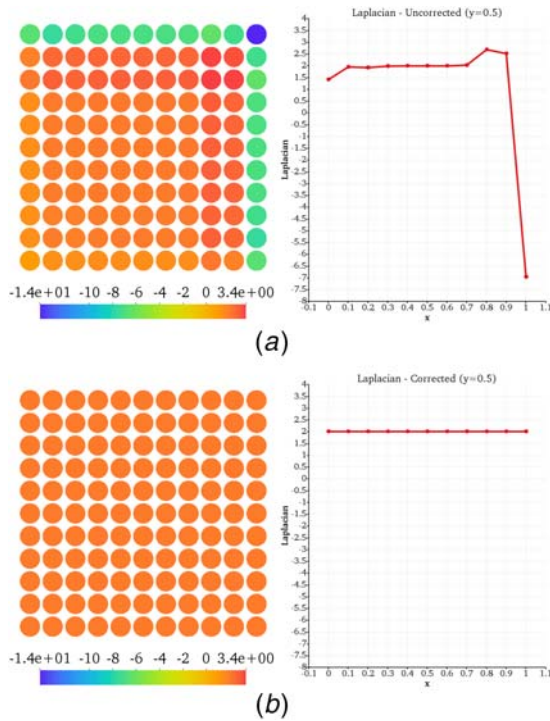
Fig. 3 Left: particle configuration. Right: Laplacian @ $y = 0.5$, $h = 3\Delta x$. (a) $\nabla^2\left(\frac{1}{2}(x^2 + y^2)\right)$ uncorrected Laplacian and (b) $\nabla_1^2\left(\frac{1}{2}(x^2 + y^2)\right)$ corrected Laplacian (our method).

with $m, n, o, p,$ and q being the indices used for the Einstein notation. In 3D, the above system is a 6×6 matrix where the components of the solution vector correspond to the entries of $\mathbf{L}_i$ (which is in result a function of $\mathbf{A}_i = A_i^{kmn}\mathbf{e}_k \otimes \mathbf{e}_m \otimes \mathbf{e}_n$ and $\boldsymbol{\delta}_i = \delta_i^{mn}\mathbf{e}_m \otimes \mathbf{e}_n$).

Using this correction, we thus modify Equation (29) to

$$c_i \frac{DT_i}{Dt} = \sum_{j \in \mathcal{N}_{FS}(i)} \left[\frac{4}{\rho_i}\left(\frac{k_i k_j}{k_i + k_j}\right)(\mathbf{L}_i : \mathbf{e}_{ij} \otimes \nabla_i W_{ij})\left(\frac{T_i - T_j}{r_{ij}} - \mathbf{e}_{ij} \cdot \nabla_i T_i\right)V_j\right]$$

(33)

here, k_i or k_j is defined to be the thermal conductivity of the fluid or solid, depending on which domain the SPH particles is defined to be within.

Although the above correction seems promising for many situations, the method carries a drawback. For a correction to exist, a particle requires at least one neighboring particle in each quadrant with respect to itself. Thus, in 3D, at least eight neighbors are required. A simple work around for particles where the correction is not defined is to resort back to Eq. (29).

3.3 Finite Element Method.

Previous effort regarding modeling solids via SPH were made in Refs. [29–31]. The main weakness of such formulations were stability and consistency. Since the solid domain of our problem is assumed to involve a stiff material (with stiffness being on the order of $100\,\text{GPa}\,\text{s}$), the fluid domain and the solid domain would require timesteps with large discrepancies, and renders modeling the whole domain with SPH difficult.

The FEM is a well-established method for discretizing PDEs and is adequate for modeling solid mechanics problems; thus is used to model the solid substrate in our problem. Each timestep, after the temperature field and the velocity/position field is updated, a linear-quasi-static thermo-elasticity problem is solved within the solid domain. Writing the weak form of the proposed problem:

$$\int_{\Omega_s} \boldsymbol{\sigma}_s(\mathbf{v}) : \boldsymbol{\varepsilon}(\bar{\mathbf{v}})\, d\Omega = \int_{\Omega_s} \mathbf{f} \cdot \bar{\mathbf{v}}\, d\Omega + \int_{\Gamma_s} \boldsymbol{\sigma}_s \mathbf{n} \cdot \bar{\mathbf{v}} d\Gamma$$
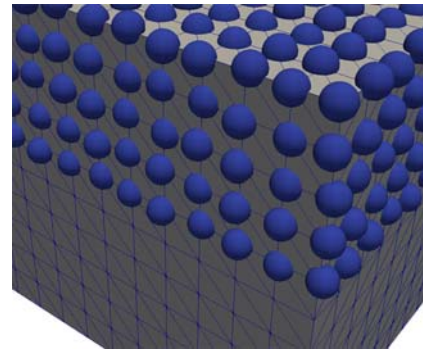
(34)

Fig. 4 SPH particles placed on top of finite element nodes

$$\boldsymbol{\sigma}_s(\mathbf{v}) = \lambda\left(\nabla \cdot \mathbf{v} - \alpha \Delta T\left(3 + 2\frac{G}{\lambda}\right)\right)\mathbf{1} + 2G\boldsymbol{\varepsilon}(\mathbf{v})$$

(35)

$$\boldsymbol{\varepsilon}(\mathbf{v}) = \frac{1}{2}\left(\nabla \mathbf{v} + (\nabla \mathbf{v})^T\right)$$

(36)

where $\mathbf{v}$ is the solution (displacement field) of the problem, $\bar{\mathbf{v}}$ is an arbitrary test function defined over the mesh, and ΔT (temperature change), $\boldsymbol{\sigma}_s \mathbf{n}|_{\Gamma_s}$ (traction boundary conditions) are values defined over Ω_s and Γ_s, respectively, and are precalculated from the SPH scheme. For simplicity, the formulation is chosen to be quasi-static. This is under the assumption that the impact speed is comparably smaller than the speed of the shock waves traveling through the solid.

The weak form above is then discretized via an isoparametric mapping with linear shape functions, and is represented as a set of linear equations involving the displacement of the nodes:

$$\mathbf{K}\mathbf{v} = \mathbf{f}$$

(37)

where $\mathbf{v}$ is the displacement field, $\mathbf{K}$ is the stiffness matrix, and $\mathbf{f}$ is computed with the inputs (temperature, force) subjected to the solid mesh. The displacement field is then post-processed to obtain the desired stress distributions. Detailed solution procedures are beyond the scope of this paper, and we refer to well-known literature such as Refs. [32,33] for details.

4 Numerical Algorithm

The above equations are solved explicitly for each field, similar to the formulations found in Ref. [34]. The main numerical procedures for each time-step follow as (also depicted in Fig. 2)

(i) *Neighbor searching.*
(ii) *Solve the momentum equation for the fluid with SPH.*
(iii) *Solve the heat equation for the fluid/solid with SPH.*
(iv) *Solve the mechanical response of the solid with FEM.*

4.1 SPH-FEM 1-Way Coupling.

As seen in Fig. 2, the information obtained from the SPH solution is fed into the FEM solver, in a 1-way coupled fashion. This is obtained by placing a grid of SPH particles on top of the finite element nodes (Fig. 4) where relevant. The FEM solver takes the inputs (pressure field/viscous forces/temperature) and then solves the thermoelasticity problem stated earlier.

4.2 Neighbor Searching.

Many particle methods, including SPH, rely on *Neighbor Searching* algorithms before computing the interactions between the particles. Here, we employ the neighbor search algorithm found at github,[2] which is a variant of the *Compact Hashing* algorithm developed in Ref. [35].

---

[2] Koschier, D., 2017, "Compactnsearch," https://github.com/thinks/poisson-disk-sampling

4.3 Particle Interaction. In order to compute the correction matrices and the diffusion term used in δ-SPH, several passes (the normalized density gradients, such as $\langle \nabla_1 \rho_i \rangle$ and the normalization matrices $\mathbf{L}_i$ and $\mathbf{B}_i$ need to be computed first) are conducted over the particles. The linear algebra library [36] was used to solve the 6×6 matrices involved in the second-derivative renormalization matrices ($\mathbf{L}_i$).

4.4 SPH-FEM Coupling and Thermoelasticity. A finite element mesh is defined over the solid domain, where the nodes coincide with the SPH particles. "Sensor Particles" that are located near the surface of the solid directly feed the observed temperature and forces to the finite element nodes. This input can be regarded as the corresponding nodal loading. The open-source FEM library by Alnæs et al. [37] was used to define and solve a thermoelasticity problem.

4.5 Initial Placement. To remove the *aliased* edges of a simple-rejection-sampled Cartesian placement, the initial particle representation of the fluid droplet was created using a 3D Poisson sampling algorithm by Hinks.[3]

The SPH particles representing the solid domain were placed using a simple Cartesian placement. Before the first timestep, the mass of each SPH particle is assigned using the number density:

$$m_i = \frac{\rho_0}{\sum_{j \in \mathcal{N}(i)} W_{ij}} \quad (38)$$

5 Convergence Study

5.1 Heat Equation With Consistent Operators. To highlight the effectiveness of the consistent operators, we compare the results to the inconsistent one by solving a (dimensionless) 1D transient heat equation. A uniform rod of length $L = 1$ and initial temperature distribution $T(x, t = 0) = 0$, $x \in [0, 1]$ is placed between two walls with constant temperature $T_{left} = 0$, $T_{right} = 1$ (Fig. 5). This is an interesting problem, since at $(x, t) = (0, 0)$, the solution is discontinuous.

The analytical time-dependent solution for this problem is given by

$$T_{analyitcal}(x, t) = 1 - Erf\left(\frac{x}{2\sqrt{t}}\right) \quad (39)$$

We compare the solutions obtained by using the formulation given in Refs. [24,28] by solving the above transient 1D heat transfer problem until $t = 0.03$ (Fig. 6) with three different discretization scales (80 nodes, 160 nodes, and 320 nodes) and with smoothing radius $3\Delta x$. We observe convergence from the corrected operators, in contrast to the conventional operators. This is a well-known issue when solving the heat equation with SPH, since the conventional operators assume sufficient amount of smoothness of the solution.

5.2 SPH-FEM Momentum Coupling. We now justify the approach regarding heat-transfer and mechanical coupling between SPH/FEM.

We verify the 1-way momentum coupling scheme described earlier by considering a steady-state 2D Poiseuille flow. Finite elements were used to represent the solid boundaries, while SPH particles represented the Newtonian fluid (Fig. 7). Viscosity of the fluid will cause shear on the walls, where the analytical steady-state velocity profile is given by

$$v_x(y) = (H^2/2\mu)\left(-\frac{dP}{dx}\right)\left(\frac{y}{H}\left(1 - \frac{y}{H}\right)\right) \quad (40)$$
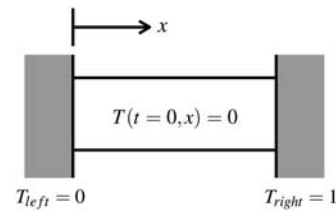
[3]Hinks, T., 2015, "Poisson Disc Sampling," https://github.com/thinks/poisson-disk-sampling

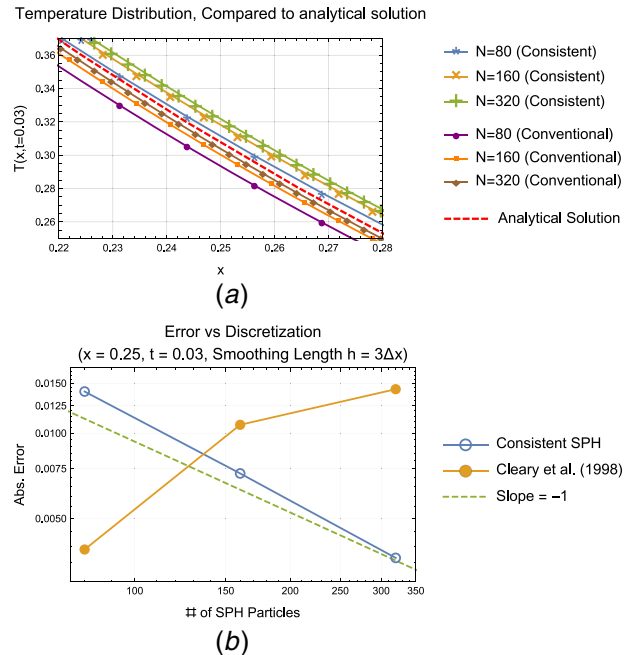**Fig. 5   1D transient heat transfer problem schematic**

Fig. 6   1D transient heat transfer problem @ $t = 0.03$: (a) $T(t = 0.03, x)$ and (b) error analysis
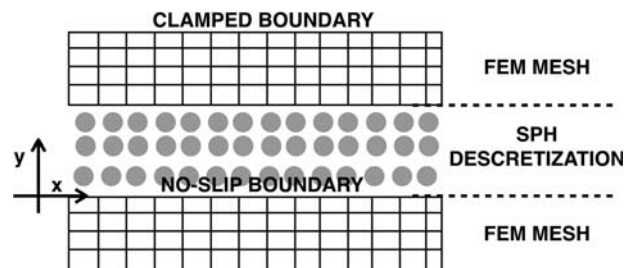

Fig. 7   Poiseuille flow shear transfer test

where H is the distance between the two plates. The analytical shear stress at the wall is given by

$$\tau_{xy} = \mu \frac{\partial v_x}{\partial y} \quad (41)$$

For the test, we use $H = 1$, $\mu = 0.001$, $\partial p/\partial x = 10$, with periodic boundary conditions on the inlet/outlet. The thickness of the wall modeled with finite elements was chosen to be $T = 0.25$. All the y-direction degree of freedoms on the finite element mesh were enforced to be 0 in order to rule out any volumetric deformations. Then, the average stress throughout the finite element domain was computed by

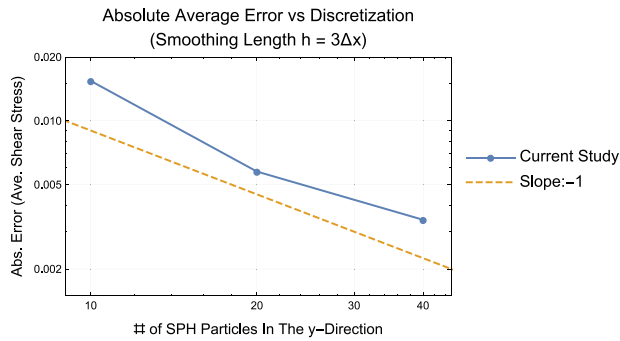$$\sigma_{ave} = \int_V \sigma(x, y) dV \quad (42)$$

Fig. 8 Average shear stress error

and was compared (Fig. 8) against the analytical value ($\tau_{xy} = 0.02$ from Eq. (40)). The results indicate that the coupling technique is suitable to model consistent momentum transfer between the solid and the fluid.

6 Numerical Example

6.1 Thermal Droplet Impact Case. A numerical example involving a droplet with high-temperature impacting a low-temperature surface was performed. Approximately 2×10^5 particles were used to represent the droplet and the solid domain. The solid substrate was clamped down with Dirichlet boundary conditions on its four sides, and was assumed to be thermally insulated from the surrounding air.

6.2 Fluid Properties.

- $\rho_0 = 1000$ (kg/m^3) (rest density)
- $T_{0,f} = 100$ ($^\circ C$) (initial temperature)
- $c_f = 4000$ (J/K kg) (specific heat)
- $k_f = 0.6$ (W/m K) (thermal conductivity)
- $\mu_f = 0.0003$ (Pa s) (dynamic viscosity of fluid)
- $c_0 = 500$ (m/s) (sound of speed)
- $D = 0.1$ (mm) (diameter of droplet)
- $v_0 = 50$ (m/s) (impact velocity)
- $s = 1 \times 10^6$ (N) (surface tension coefficient)
- $t_c = 2.0 \times 10^{-6}$ (s) (characteristic time)

Note: The below parameters represent the properties of water, in general.

6.3 Solid Properties.

- $L = 2$ mm $\times$ 2 mm $\times$ 0.26 mm
- $\rho_s = 3950$ (kg/m^3) (specific mass)
- $T_{0,s} = 20$ ($^\circ C$) (initial temperature)
- $\mu_s = 0.0003$ (Pa s) (dynamic viscosity of solid/fluid interface)
- $c_s = 900$ (J/kg K) (specific heat)
- $k_s = 10$ (W/m K) (thermal conductivity)
- $E = 300$ (GPa)
- $\nu = 0.21$ (Poisson's ratio)
- $\alpha = 8.1 \times 10^{-6}$ (thermal expansion coefficient)

Note: The below parameters broadly represent the properties of typical alumina.

6.4 General Parameters.

- $\Delta x = 2.5 \times 10^{-6}$ (m) (particle stencil)
- $h = 3\Delta x$ (m) (smoothing length)
- $\gamma = 7$ (tait EOS parameter)
- $dt = 2.5 \times 10^{-10}$ (s) (timestep)

6.5 Analysis. Here, we have demonstrated an useful example regarding the usage of the computational framework we have introduced in this paper. In detail, Fig. 9 shows the temperature of the droplet along with the evolution of the droplet geometry. Figure 10 shows the temperature distribution of the substrate at $t/t_c = 1.75$.

Initially, the heat transfer is confined within the small contact patch of the droplet, where the temperature arises locally. The timescale of the impact limits the increase of temperature of the solid at deeper depths, as seen in Fig. 12. We observe that for the timescale of interest, the heat transfer occurring between the fluid and the solid dominates the temperature increase in the solid.

The stress within the substrate increases with time (Fig. 11), as the droplet breaks spreads over the surface. The stress is the largest near the surface of the substrate, as seen in Fig. 12. This is due to the large heat and momentum transfer between the droplet and the surface at the contact patch (Fig. 11). The contact patch between the droplet and the substrate expands radially.

We focus on time $t/t_c = 1.75$, where the droplet is fully deposited onto the substrate (as shown in Fig. 9). Figure 10 shows the surface
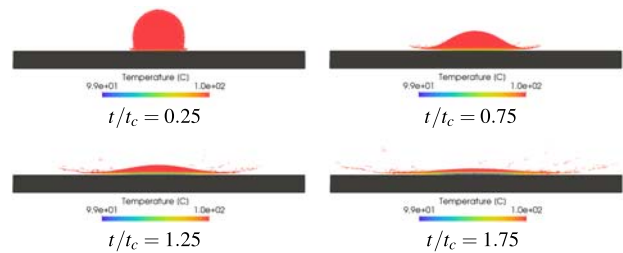

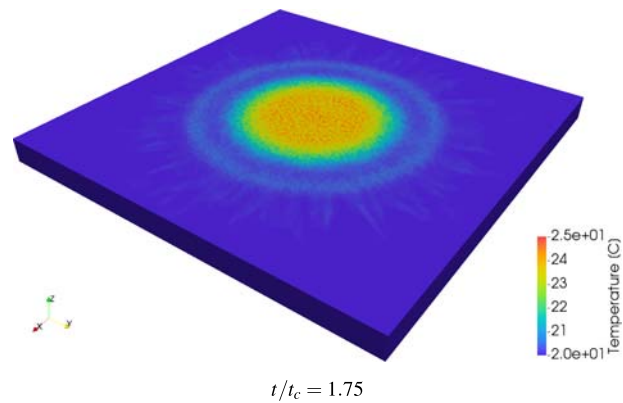**Fig. 9 Evolution of a fluid droplet impacting the substrate**

Fig. 10 Temperature distribution on the substrate surface at $t/t_c = 1.75$
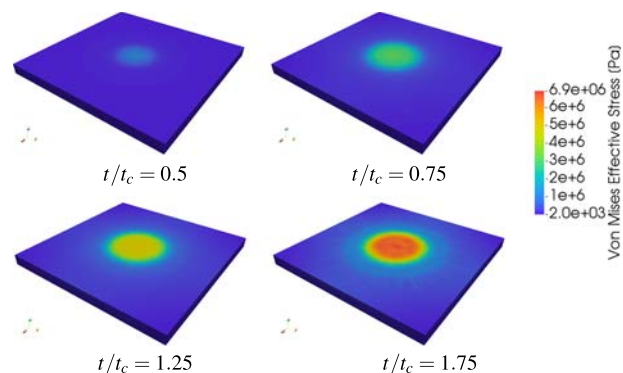

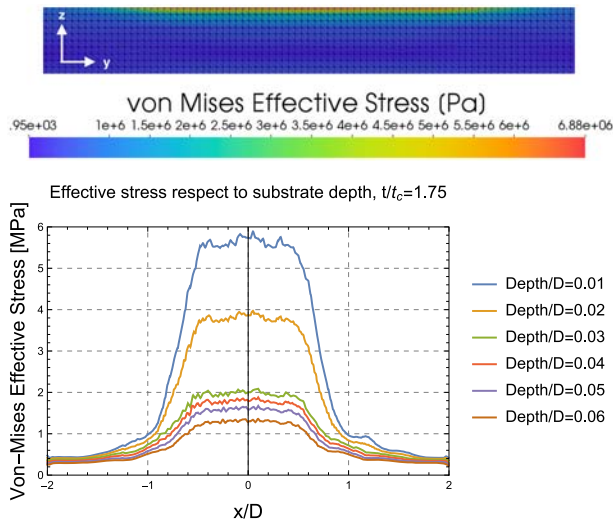**Fig. 11 Stress (Von-Mises) distribution on the substrate surface**

Fig. 12 Stress on the substrate with respect to depth ($t/t_c = 1.75$, $x = 0$)
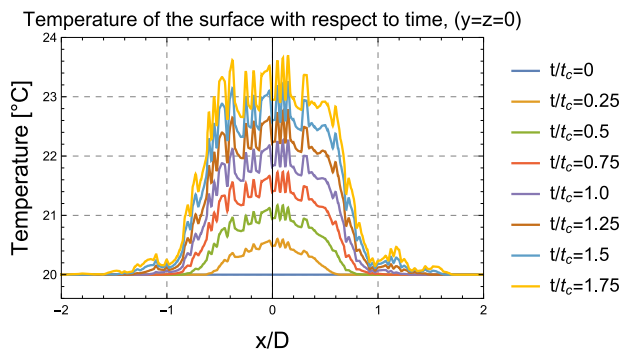

Fig. 13 Temperature evolution on substrate surface, with respect to time

temperature distribution, which indicates that the majority of the heat transfer is made through the initial contact patch with a diameter of roughly 0.6 times the initial droplet diameter (0.06 mm) (Fig. 13). The effective (Von-Mises) stress experienced by the substrate along the cross-section is depicted in Fig. 12, which shows the concentrated stress near the surface (Fig. 14).

For the homogeneous material (alumina) in consideration for the current example, we can predict that no type of failure will occur, since the stress levels shown in Fig. 12 are well below the known failure criterion. On the other hand, for tailor-made substrates obtained by mixing specific functional microparticles into a binding matrix, this type of concentrated stresses confined to the surface will usually result in a delamination-type defect [38]. This is a well-known micromechanical pheonomenon, and is due to the stress concentrations that occur between the interface of the functional particle and the matrix. The stress concentration factors may become extremely high in certain situations, as seen in Ref. [39]. Thus, for such applications, it is critical to first find the stress concentration factor by experiments or computational methods via RVE (representative volume element) methods before making a conclusion regarding the design of the deposition process.

7 Discussion

7.1 Summary. An enhanced formulation of SPH was coupled with a finite element solver to deliver a practical tool that can quickly simulate the thermo-mechanical stresses occurring on the substrate of such processes. The modified corrected SPH scheme robustly handles various starting configurations, including free surfaces, while providing improved accuracy over its conventional counterpart. The coupling between SPH and FEM was achieved via staggering of SPH particles on top of finite element nodes, where the physics observed by the SPH particles were directly enforced on the corresponding finite element node. To summarize, the resulting framework allows:

- Fast and accurate modeling of Newtonian fluid droplets.
- Thermal and mechanical coupling between fluids with free-surfaces and solids.
- Removal of timestep limitations imposed due to different CFL conditions for the solid and fluid.

As noted earlier, the above aspects are all very useful features to have when conducting numerical experiments on droplet deposition manufacturing techniques. Mesh-based approaches require frequent re-meshing, and may become computationally extremely expensive.

Overall, a rapid simulation framework that can provide useful insight regarding the induced mechanical stresses for droplet-based additive manufacturing was developed. With an example demonstrating a droplet impacting a solid surface, we have shown that the framework is capable of providing useful insights that may be sometimes hard to obtain by purely experimental methods. Justification of the framework was also given by performing convergence
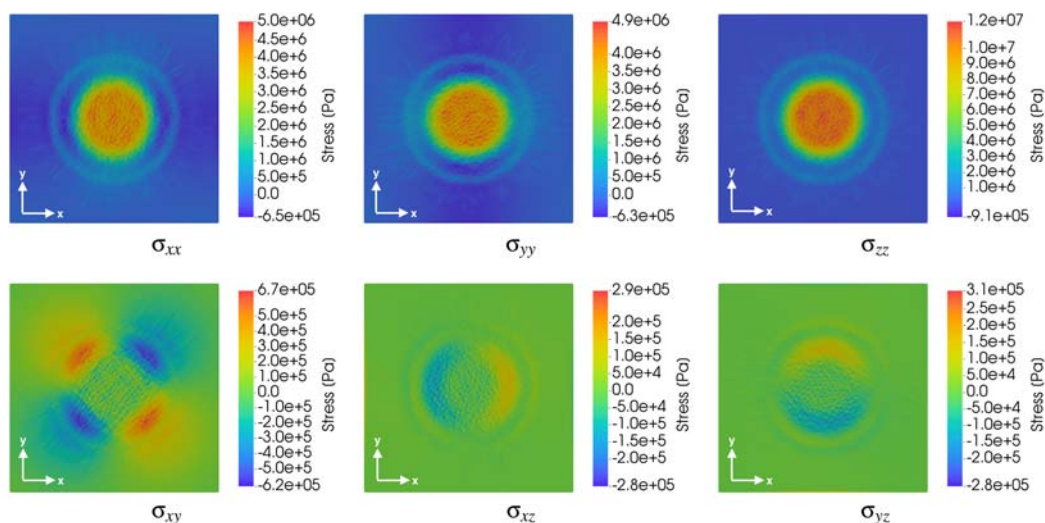

Fig. 14 Stress components, $t/t_c = 1.75$

analysis on the thermal/mechanical coupling methods. Since the numerical results are derived from a direct numerical simulation of the proposed continuum problem, the various material/mechanical parameters used in the simulation can be altered freely to suit the users' needs.

7.2 Limitations. Although the method assumes the fluid model to be homogeneous, this is not necessarily the case for many emerging additive manufacturing methods. In some applications, specifically tailored micro/nano materials are mixed with a base fluid [2,8,9,40,41]. Often, these are referred to as "functionalized" inks.

In many cases, mixing functional powders into the solvent forces the ink to have shear-thinning properties, along with a yielding stress. The mechanical behavior of such inks can usually be modeled with non-Newtonian fluid models, one being the popular Herschel–Bulkley fluid model. For this model, the shear stress of a fluid can be written as

$$\tau = \tau_y + K\dot{\gamma}^n \tag{43}$$

where τ_y is the yield stress, $\dot{\gamma}$ is the effective shear rate, and K, n are parameters to be fitted. Many previous work on DIW fabrication methods have successfully employed [7,42] the Herschel Bulkley model to explain the mechanical behaviour of these inks. In numerical implementations, the "Regularized Herschel Bulkley" model is frequently used, where a shear-rate-dependent effective viscosity is used for the viscosity term in the Navier–Stokes equations:

$$\tau = 2\mu_{eff}(\dot{\gamma}), \quad \mu_{eff}(\dot{\gamma}) = \begin{cases} k\dot{\gamma}_0^{n+1} + \tau_0\dot{\gamma}_0^{-1}, & \dot{\gamma} \leq \dot{\gamma}_0 \\ k\dot{\gamma}_0^{n-1} + \tau_0\dot{\gamma}_0^{n-1}, & \dot{\gamma} \geq \dot{\gamma}_0 \end{cases} \tag{44}$$

For unyielded regions within the fluid, the high effective viscosity will make the fluid behave similar to a rigid body. For yielded regions, the viscosity will be several magnitudes smaller compared to the unyielded regions. Therefore, with an explicit time-stepping approach with SPH, the problem becomes very difficult to solve, and an implicit time stepping scheme must be implemented to alleviate the difficulties. To our best knowledge, no such schemes have been devised specifically for non-Newtonian fluids with SPH. This topic is currently under investigation by the authors.

Acknowledgment

References

[1] Chun, J.-H., Passow, C. H., and Suh, N. P., 1993, "Droplet-Based Manufacturing," CIRP ANNALS-Manuf. Technol., **42**(1), pp. 235–238.
[2] Minemawari, H., Yamada, T., Matsui, H., Tsutsumi, J., Haas, S., Chiba, R., Kumai, R., and Hasegawa, T., 2011, "Inkjet Printing of Single-Crystal Films," Nature, **475**(7356), p. 364.
[3] Cui, L., Li, Y., Wang, J., Tian, E., Zhang, X., Zhang, Y., Song, Y., and Jiang, L., 2009, "Fabrication of Large-Area Patterned Photonic Crystals by Ink-Jet Printing," J. Mater. Chem., **19**(31), pp. 5499–5502.
[4] Delaporte, P., and Alloncle, A.-P., 2016, "Laser-Induced Forward Transfer: A High Resolution Additive Manufacturing Technology," Optics Laser Technol., **78**, pp. 33–41.
[5] Willis, D. A., and Grosu, V., 2005, "Microdroplet Deposition by Laser-Induced Forward Transfer," Appl. Phys. Lett., **86**(24), p. 244103.
[6] Adrian, F., Bohandy, J., Kim, B., Jette, A. N., and Thompson, P., 1987, "A Study of the Mechanism of Metal Deposition by the Laser-Induced Forward Transfer Process," J. Vacuum Sci. Technol. B: Microelectron. Process. Phenomena, **5**(5), pp. 1490–1494.
[7] Compton, B. G., and Lewis, J. A., 2014, "3D-Printing of Lightweight Cellular Composites," Adv. Mater., **26**(34), pp. 5930–5935.
[8] Choi, S., Stassi, S., Pisano, A. P., and Zohdi, T. I., 2010, "Coffee-Ring Effect-Based Three Dimensional Patterning of Micro/Nanoparticle Assembly With a Single Droplet," Langmuir, **26**(14), pp. 11690–11698.
[9] Choi, S., Jamshidi, A., Seok, T. J., Wu, M. C., Zohdi, T. I., and Pisano, A. P., 2012, "Fast, High-Throughput Creation of Size-Tunable Micro/Nanoparticle Clusters via Evaporative Self-Assembly in Picoliter-Scale Droplets of Particle Suspension," Langmuir, **28**(6), pp. 3102–3111.
[10] Kattamis, N. T., Purnick, P. E., Weiss, R., and Arnold, C. B., 2007, "Thick Film Laser Induced Forward Transfer for Deposition of Thermally and Mechanically Sensitive Materials," Appl. Phys. Lett., **91**(17), p. 171120.
[11] Bulgakov, A. V., Goodfriend, N., Nerushev, O., Bulgakova, N. M., Starinskiy, S. V., Shukhov, Y. G., and Campbell, E. E., 2014, "Laser-Induced Transfer of Nanoparticles for Gas-Phase Analysis," JOSA B, **31**(11), pp. C15–C21.
[12] Sanz, M., Walczak, M., Oujja, M., Domingo, C., Klini, A., Papadopoulou, E., Fotakis, C., and Castillejo, M., 2010, "Femtosecond Laser Deposition of TiO_2 by Laser Induced Forward Transfer," Thin. Solid. Films, **518**(19), pp. 5525–5529.
[13] Hiraoka, K., Takaishi, R., Asakawa, D., Sakai, Y., and Iijima, Y., 2009, "Surface Characterization of Polymethylmetacrylate Bombarded by Charged Water Droplets," J. Vacuum Sci. Technol. A: Vacuum Surfaces Films, **27**(4), pp. 748–753.
[14] Colagrossi, A., Antuono, M., Souto-Iglesias, A., and Izaguirre-Alza, P., 2010, "Theoretical Analysis of SPH in Simulating Free-Surface Viscous Flows". 5th International SPHERIC SPH Workshop, University of Manchester, UK, June 23–25.
[15] Antuono, M., Colagrossi, A., Marrone, S., and Lugni, C., 2011, "Propagation of Gravity Waves Through an SPH Scheme With Numerical Diffusive Terms," Comput. Phys. Commun., **182**(4), pp. 866–877.
[16] Monaghan, J. J., 1994, "Simulating Free Surface Flows with SPH," J. Comput. Phys., **110**(2), pp. 399–406.
[17] Morris, J. P., 2000, "Simulating Surface Tension With Smoothed Particle Hydrodynamics," Int. J. Numer. Methods Fluids, **33**(3), pp. 333–353.
[18] Monaghan, J., 2012, "Smoothed Particle Hydrodynamics and Its Diverse Applications," Annu. Rev. Fluid Mech., **44**, pp. 323–346.
[19] Tartakovsky, A., and Meakin, P., 2005, "Modeling of Surface Tension and Contact Angles With Smoothed Particle Hydrodynamics," Phys. Rev. E, **72**(2), p. 026301.
[20] Macia, L., Souto, I. A., Antuono, M., and Colagrossi, A., 2011, "Benefits of Using a Wendland Kernel for Free-Surface Flows". 6th International SPHERIC Workshop, June 8–10, Hamburg, Germany.
[21] Shao, S., and Lo, E. Y., 2003, "Incompressible SPH Method for Simulating Newtonian and Non-Newtonian Flows With a Free Surface," Adv. Water Resources, **26**(7), pp. 787–800.
[22] Antuono, M., Colagrossi, A., Marrone, S., and Molteni, D., 2010, "Free-Surface Flows Solved by Means of SPH Schemes With Numerical Diffusive Terms," Comput. Phys. Commun., **181**(3), pp. 532–549.
[23] Oger, G., Doring, M., Alessandrini, B., and Ferrant, P., 2007, "An Improved SPH Method: Towards Higher Order Convergence," J. Comput. Phys., **225**(2), pp. 1472–1492.
[24] Cleary, P. W., 1998, "Modelling Confined Multi-Material Heat and Mass Flows Using SPH," Appl. Math. Model., **22**(12), pp. 981–993.
[25] Cleary, P., and Monaghan, J., 1999, "Conduction Modelling Using Smoothed Particle Hydrodynamics," J. Comp. Phys., **148**, pp. 227–264.
[26] Souto-Iglesias, A., Macià, F., González, L. M., and Cercos-Pita, J. L., 2013, "On the Consistency of MPS," Comput. Phys. Commun., **184**(3), pp. 732–745.
[27] Trask, N., Maxey, M., Kim, K., Perego, M., Parks, M. L., Yang, K., and Xu, J., 2015, "A Scalable Consistent Second-Order SPH Solver for Unsteady Low Reynolds Number Flows," Comput. Methods Appl. Mech. Eng., **289**, pp. 155–178.
[28] Fatehi, R., and Manzari, M., 2011, "Error Estimation in Smoothed Particle Hydrodynamics and a New Scheme for Second Derivatives," Comput. Math. Appl., **61**(2), pp. 482–498.
[29] Antoci, C., Gallati, M., and Sibilla, S., 2007, "Numerical Simulation of Fluid–Structure Interaction by SPH," Comput. Struct., **85**(11), pp. 879–890.
[30] Gray, J., Monaghan, J., and Swift, R., 2001, "SPH Elastic Dynamics," Comput. Methods Appl. Mech. Eng., **190**(49), pp. 6641–6662.
[31] Vidal, Y., Bonet, J., and Huerta, A., 2007, "Stabilized Updated Lagrangian Corrected SPH for Explicit Dynamic Problems," Int. J. Numer. Methods Eng., **69**(13), pp. 2687–2710.
[32] Zienkiewicz, O. C., Taylor, R. L., Zienkiewicz, O. C., and Taylor, R. L., 1977, The Finite Element Method, 3, McGraw-Hill, London.
[33] Bathe, K.-J., 2006, Finite Element Procedures. Klaus-Jurgen Bathe, Prentice-Hall.
[34] Zohdi, T., 2010, "On the Dynamics of Charged Electromagnetic Particulate Jets," Arch. Comput. Methods Eng., **17**(2), pp. 109–135.
[35] Ihmsen, M., Akinci, N., Becker, M., and Teschner, M., 2011, A Parallel SPH Implementation on Multi-Core Cpus, Computer Graphics Forum, Vol. 30, Wiley Online Library, Berlin, pp. 99–112.
[36] Guennebaud, G., Jacob, B. 2010, "Eigen v3," http://eigen.tuxfamily.org
[37] Alnæs, M. S., Blechta, J., Hake, J., Johansson, A., Kehlet, B., Logg, A., Richardson, C., Ring, J., Rognes, M. E., and Wells, G. N., 2015, "The Fenics Project Version 1.5," Arch. Numer. Softw., **3**(100), pp. 9–23.
[38] Marshall, D., and Evans, A., 1984, "Measurement of Adherence of Residually Stressed Thin Films by Indentation. I. Mechanics of Interface Delamination," J. Appl. Phys., **56**(10), pp. 2632–2638.
[39] Zohdi, T. I., and Wriggers, P., 2008, An Introduction to Computational Micromechanics, Springer Science and Business Media, Berlin.
[40] Tekinalp, H. L., Kunc, V., Velez-Garcia, G. M., Duty, C. E., Love, L. J., Naskar, A. K., Blue, C. A., and Ozcan, S., 2014, "Highly Oriented Carbon Fiber–Polymer Composites via Additive Manufacturing," Compos. Sci. Technol., **105**, pp. 144–150.
[41] Fedorovich, N. E., Schuurman, W., Wijnberg, H. M., Prins, H.-J., Van Weeren, P. R., Malda, J., Alblas, J., and Dhert, W. J., 2011, "Biofabrication of Osteochondral Tissue Equivalents by Printing Topologically Defined, Cell-Laden Hydrogel Scaffolds," Tissue Eng. Part C: Methods, **18**(1), pp. 33–44.
[42] Lewis, J. A., 2000, "Colloidal Processing of Ceramics," J. Am. Ceram. Soc., **83**(10), pp. 2341–2359.